

# Knowledge-enhanced Visual-Language Pretraining for Computational Pathology

Xiao Zhou<sup>1</sup>, Xiaoman Zhang<sup>1,2</sup>, Chaoyi Wu<sup>1,2</sup>, Ya Zhang<sup>1,2</sup>,  
Weidi Xie<sup>1,2</sup>, Yanfeng Wang<sup>1,2</sup>

<sup>1</sup> Shanghai AI Laboratory

<sup>2</sup> Shanghai Jiao Tong University

<https://github.com/MAGIC-AI4Med/KEP>

zhouxiao@pjlab.org.cn, {xm99sjtu, wtzxxxwcy02, ya\_zhang, weidi,  
wangyanfeng}@sjtu.edu.cn

**Abstract.** In this paper, we consider the problem of visual representation learning for computational pathology, by exploiting large-scale image-text pairs gathered from public resources, along with the domain-specific knowledge in pathology. Specifically, we make the following contributions: (i) We curate a pathology knowledge tree that consists of 50,470 informative attributes for 4,718 diseases requiring pathology diagnosis from 32 human tissues. To our knowledge, this is the first comprehensive structured pathology knowledge base; (ii) We develop a knowledge-enhanced visual-language pretraining approach, where we first project pathology-specific knowledge into latent embedding space via language model, and use it to guide the visual representation learning; (iii) We conduct thorough experiments to validate the effectiveness of our proposed components, demonstrating significant performance improvement on various downstream tasks, including cross-modal retrieval, zero-shot classification on pathology patches, and zero-shot tumor subtyping on whole slide images (WSIs). All codes, models and the pathology knowledge tree will be released to the research community.

**Keywords:** Pathology knowledge · Visual-language pretraining

## 1 Introduction

Pathology diagnosis is currently the golden standard for examining various diseases in clinical applications, for example, in the diagnosis of neoplasia and cancer [44]. In the last decade, the prosperity of deep learning on computer vision has led to the rapid development of computational pathology, for example, approaches with supervised learning [7, 34, 46, 47], and weakly supervised learning [5, 13, 32, 38]. Despite being promising, these approaches have been fundamentally limited by the scale of costly annotations. Alternatively, self-supervised pretraining on numerous unlabeled pathological images [9, 10, 26, 49] has attracted unprecedented attention, yet it still requires supervised fine-tuning for downstream deployments.

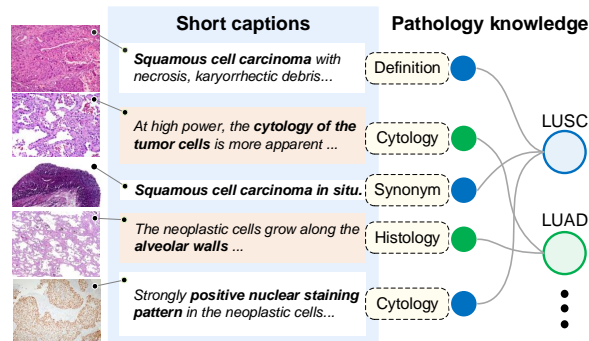


**Fig. 1:** Knowledge-enhanced pathology image-text alignment. The short caption of a pathology image crawled from public websites is typically unstructured and with varying granularities, which introduces noticeable ambiguities for image-text alignment. While the implicit structures and correlations between different image-caption pairs could be constructed by explicit disease attributes (dashed boxes), which can be well-aligned by a pathology knowledge tree. LUSC and LUAD suggest lung squamous cell carcinoma, and lung adenocarcinoma, respectively.

In the recent literature [25, 42], studies on the multimodal foundation model have demonstrated conspicuous improvement in downstream zero-shot tasks, by simply training to align visual and language embedding space on massive image-text pairs crawled from public websites. In contrast to computer vision [25, 42], representation learning in pathology requires tremendous expertise and domain knowledge. An ideal training corpus would thus consist of well-structured medical reports from the hospital, however, it is often extremely difficult to acquire, due to privacy concerns. Alternatively, recent works [23, 24, 36, 37] propose to gather large-scale image-caption pairs from public resources (PubMed [43] papers, Twitter, Youtube videos). Compared to discrete image labels, image captions from medical reports and academic articles can potentially provide more valuable medical information without the need for manual annotation.

For existing works that adopt simple contrastive learning on pathology image and caption pairs, they suffer from the following challenges: *First*, the short captions from these web-crawled image-text pairs are typically noisy, unstructured, and lack domain knowledge (Fig. 1), which can be sub-optimal for constructing high-quality pathology-specific visual representation; *Second*, the varying granularities of the free text from captions will inevitably introduce ambiguities when aligning with images, thus causing the model to be highly sensitive to the used text prompts during the inference stage [36]. Thus, effectively harnessing the potential of such web-crawled data remains to be a challenge.

In this paper, to tackle the above challenges, we anticipate that introducing pathology knowledge is of great significance to make up for the deficiency of short image captions. To this end, we make the following contributions: (i) We curate a pathology knowledge tree, **PathKT**, by collecting 50,470 informative pathological attributes of 4,718 diseases in 32 tissues from publicly available

educational resources and OncoTree<sup>3</sup> [31]. (ii) We propose a novel knowledge encoder pretraining approach, that projects the attributes of each disease from PathKT into latent embedding space, where the attributes of the same disease, including disease synonyms, definitions, histology, and cytology features, share similar representations. (iii) We develop a knowledge-enhanced pretraining (**KEP**) approach to align pathology visual-language representations, which freezes the knowledge encoder and continuously injects domain-specific knowledge into the image-text embedding space. To demonstrate the effectiveness of our proposed approach, we conduct thorough experiments on three downstream tasks, including retrieval on three pathological image-caption datasets, zero-shot patch classification on eight datasets of patch-level pathology images, and zero-shot WSI tumor subtyping on three datasets from The Cancer Genome Atlas (TCGA)<sup>4</sup>. Quantitative experiments suggest that knowledge guidance can significantly enhance the performance across different tasks.

## 2 Related work

**Vision-Language Pretraining (VLP).** Current vision-language pretraining approaches are typically categorized into two groups. The first group, referred to as two-stream approaches [42, 52], involves using two separate encoders to extract features for visual and textual data, respectively. The second group, known as single-stream methods [12, 29], utilizes a cross-modal fusion encoder to enhance interactions between vision and text features. In the field of medical VLP, existing methods mainly adopt the two-stream approach [8, 14, 21, 35, 40, 58, 60]. Despite the valuable contributions of these methods, the reliance on data-driven representation learning restricts the utilization of systematic and structured medical knowledge, leading to less than professional diagnosis.

**VLP in Computational Pathology.** In the recent literature, Huang et al. proposed a pathology VLP model named PLIP [23] and released OpenPath that contains 200K image-caption pairs from the social media of Twitter and other public resources. To extend the pathology data scale, Ikezogwo et al. curate Quilt1m [24] with over one million histopathology image-text pairs by capturing keyframes and speech from YouTube videos. In addition to evaluating the zero-shot classification on patch-level pathology images, Lu et al. propose MI-Zero [37] and CONCH [36] to extend the transfer ability of pathology VLP models on gigapixel whole slide images (WSIs). In contrast to these existing work, that finetunes a CLIP [42] or CoCa [56] on pathology image-caption pairs, we propose to first train a pathology-specific knowledge encoder, and use it to guide visual-language representation learning.

**Medical Knowledge-enhanced Learning.** In the medical community, leveraging external medical knowledge to enhance deep learning models has become an increasingly important topic [50, 51, 59]. Generally, existing approaches can

<sup>3</sup> <https://oncotree.info/>

<sup>4</sup> <https://portal.gdc.cancer.gov/>

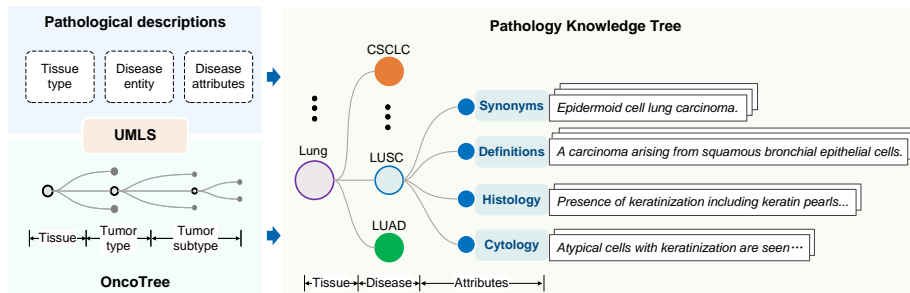


**Fig. 2:** The construction of pathology knowledge tree. OncoTree is adopted as the base architecture to construct the PathKT. The tissue types, disease entities, and attributes are first extracted from pathological descriptions, in which cancers are then matched to OncoTree based on their tissue types and tumor types/subtypes using UMLS CUIs. Moreover, non-tumor diseases are added to the knowledge tree according to their tissue types. Finally, the pathology knowledge tree integrates 4718 diseases from 32 tissues, with each disease containing various synonyms, definitions, and histological and cytological features. CSCLC, LUSC, and LUAD in this figure suggest combined small cell lung cancer, lung squamous cell carcinoma, and lung adenocarcinoma, respectively.

be categorized based on the ways of using medical knowledge: model-based approaches [16, 22] adopts the prior knowledge of radiology or diagnosis summarized by doctors to design algorithms; and input-based methods [15, 33, 54, 55] directly exploit knowledge as the external input to guide representation training. However, most of these works are focused on the analysis of chest X-rays.

### 3 Methods

Our primary goal is to leverage structured pathology knowledge to enhance visual-language representation learning. To start with, we construct a **Pathology Knowledge Tree**, termed as **PathKT**, that consists of 50,470 informative attributes of 4718 diseases from 32 human tissues (Sec. 3.1). We then train a knowledge encoder that projects the structured pathology knowledge into an embedding space (Sec. 3.2). We further employ the knowledge encoder to guide visual-language pretraining for computational pathology, termed as KEP (**K**nowledge-**E**nhanced **P**re-training, Sec. 3.3).

#### 3.1 PathKT Construction

Here, we detail the procedure for building up a pathology knowledge tree with various online sources, which will be further used for knowledge encoding.

**Knowledge Source.** We collect pathology-specific knowledge from publicly available educational resources, such as text books, professional websites, and structured databases (OncoTree<sup>3</sup>). Specifically, we extract pathological descriptions of 884 tumor subtypes from OncoTree and 4360 diseases from text books

**Table 1:** Statistics of the dataset for knowledge encoder pretraining. Syn., Def., His. and Cyt. denote synonyms, definitions, histological and cytological features.

Attributes	Syn.	Def.	His.	Cyt.	All
# Tissue	32	32	30	30	32
# Disease entity	3,348	4,661	3,558	1,117	4,718
# Attributes	30,950	10,097	3,558	1,117	50,470

and professional websites, including all domain knowledge required for diagnosis in clinical scenarios, *i.e.*, disease name/ synonyms, definitions, histological features, and cytological features.

**Knowledge Tree Construction.** We structure these knowledge sources into a knowledge tree by expanding the OncoTree, as shown in Fig. 2. OncoTree is a tree-structure cancer classification system [31], which consists of 884 tumor subtypes from 32 tissues, with each type of tumor linked to a Concept Unique Identifier (CUI) from Unified Medical Language System (UMLS) [2]. Specifically, we first extract tissue types, disease entities, and disease attributes from pathological descriptions of 4360 diseases, in which 168 cancers are found overlapped with OncoTree by using SciSpacy package [41] to link the UMLS CUIs. The rest 4192 diseases are then added to the knowledge tree according to their tissue types. After deduplication and noise reduction (358 diseases without any informative descriptions are deleted), all diseases are organized into the corresponding tissues. The final histopathology knowledge tree contains 4718 diseases from 32 tissues. The attributes of each disease node are constructed by a varying number of synonyms, definitions, and histological and cytological descriptions, as shown in Tab. 1. In the final PathKT, for instance, the tissue node of the lung connects all lung diseases, including combined small cell lung cancer (CSCLC), lung squamous cell carcinoma (LUSC), and lung adenocarcinoma (LUAD), etc. The LUSC node connects four kinds of attributes, shown in Fig. 2.

### 3.2 Pathology Knowledge Encoding

In this section, we describe details for projecting tree-structure pathological knowledge into a latent embedding space, by training a knowledge encoder. Specifically, we align different disease entities with their corresponding free-text attributes via metric learning, such that, the synonyms, definitions, and corresponding histological/cytological features are close in the embedding space. As a consequence, the model, to a large extent, can link the pathology images to their implicit disease labels during the visual-language pretraining since the free-form text descriptions in image-text pairs may contain disease attributes, such as pathological features and disease definitions, which have already been aligned with disease names/synonyms. Therefore, the alignment of pathology knowledge can help the model link to the disease entities for better performance during diagnosis.

**Problem Setting.** Given a set of disease entities with their corresponding attributes,  $\mathcal{D} = \{(d_1, \mathbf{a}_1), \dots, (d_n, \mathbf{a}_n)\}$ , where  $d_i$  denotes the  $i$ -th disease entity,

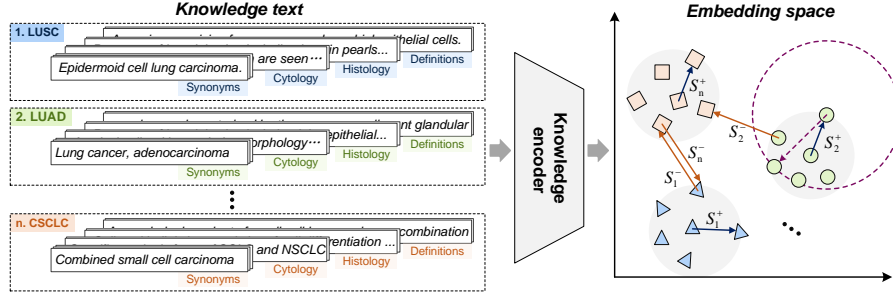


**Fig. 3:** Knowledge encoder pretraining based on metric learning.  $n$  disease entities and each with  $k$  attributes, including disease synonyms, definitions, cytology and pathology features, construct a mini-batch (left part of the figure), which are fed to a knowledge encoder for pretraining. In the embedding space (right part of the figure), the markers in different shapes represent the embeddings of attributes of different diseases.  $S_i^+$  suggests the max-min positive attribute similarity within the  $i$ -th disease, while  $S_i^-$  denotes the maximal attribute similarity between the  $i$ -th disease and other diseases. The goal of metric learning is to increase  $S_i^+$  and meanwhile decrease  $S_i^-$ . The purple-dashed arrow and circle denote the minimal positive attribute similarity in the second class and the hypersphere it spans.

and  $\mathbf{a}_i = \{a_i^1, \dots, a_i^k\}$  refer to the associated  $k$  attributes, both disease and attributes are represented in the format of natural language. Note that, for different disease entities,  $k$  also varies, our goal here is to train a model that satisfies:

$$\text{sim}(\Phi_k(a_i^p), \Phi_k(a_i^q)) \gg \text{sim}(\Phi_k(a_i^p), \Phi_k(a_j^t)), \quad i \neq j, \quad (1)$$

where  $\Phi_k(\cdot)$  denotes the knowledge encoder,  $\text{sim}(\cdot, \cdot)$  refers to the similarity,  $a_i^p$ ,  $a_i^q$  and  $a_j^t$  refer to the randomly sampled attributes from the  $i, j$ -th disease entity. Intuitively, the knowledge encoder enables the attributes of the same disease to be pulled together, while attributes from different diseases are pushed apart.

**Training.** In order to achieve the objective defined in Eq. 1, metric learning is exploited to construct an embedding space where the representations of intra/inter-class instances are clustered/separated. In specific, given a mini-batch that contains  $n$  random diseases and each with  $k$  attributes, we denote the normalized embedding for the  $p$ -th attribute of  $i$ -th disease as:  $\mathbf{z}_p^i = \Phi_k(a_i^p) / \|\Phi_k(a_i^p)\|$ , where  $\Phi_k(a_i^p)$  represents the output embedding from knowledge encoder. We adopt the recently proposed AdaSP loss [61], which finds out a max-min positive similarity (Fig. 3) and then shapes a loss with the maximal negative similarity:

$$\mathcal{L}_{\text{metic}} = \frac{1}{n} \sum_{i=1}^n \log \left( 1 + e^{(S_i^- - S_i^+)/\tau} \right), \quad (2)$$

where  $\tau$  is a temperature parameter.  $S_i^+$  and  $S_i^-$  denote the max-min positive and the maximal negative similarity, which can be computed by the soft version:

$$S_i^+ = \max_p \min_q \langle \mathbf{z}_p^i, \mathbf{z}_q^i \rangle \approx \tau \log \left( \frac{1}{\sum_{p=1}^k \sum_{q=1}^k e^{-\frac{\langle \mathbf{z}_p^i, \mathbf{z}_q^i \rangle}{\tau}}} \right) \quad (3)$$

$$S_i^- = \max_{j,p,q} \langle \mathbf{z}_p^i, \mathbf{z}_q^j \rangle \approx \tau \log \left( \sum_{p=1}^k \sum_{j=1, j \neq i}^n \sum_{q=1}^k e^{\frac{\langle \mathbf{z}_p^i, \mathbf{z}_q^j \rangle}{\tau}} \right) \quad (4)$$

where  $\langle \cdot \rangle$  represents the cosine similarity, the details about the soft version can be found in Supplementary Materials.

**Discussion.** The conventional triplet loss [20] with batch hard mining strategy is widely adopted in metric learning, while it is not suitable in our case due to the following two reasons: *First*, in the pathology knowledge, each disease entity is associated with at most four types of attributes, the text descriptions of different attribute types might reveal significant divergence, which causes a large intra-class variation, marked by the purple dashed circle in Fig. 3, during training. *Second*, the fine-grained diseases might share high similarities, such as tumor subtypes: breast invasive ductal carcinoma and breast invasive lobular carcinoma, which cause low inter-class variations during training. When a mini-batch meets these two conditions, traditional triplet loss that enforces the instance similarities could typically produce the bad local minima of optimization [53], which, therefore, undermines the metric learning.

### 3.3 Pathology Knowledge Enhanced Pretraining

In this section, we present a simple yet effective pretraining approach, termed KEP, that leverages the established knowledge encoder to guide visual-language pretraining for computational pathology.

**Visual-Language Pretraining.** Given paired image and captions, denoted as  $\mathcal{F} = \{(x_1, c_1), \dots, (x_n, c_n)\}$ , our goal is to construct a visual-language embedding space from paired image-text data, that satisfies:

$$\text{sim}(\Phi_v(x_i), \Phi_t(c_i)) \gg \text{sim}(\Phi_v(x_i), \Phi_t(c_j)), \quad i \neq j, \quad (5)$$

where  $\Phi_v(\cdot)$  and  $\Phi_t(\cdot)$  denote the visual and the textual encoder, respectively.  $\text{sim}(\cdot, \cdot)$  refers to the similarity. In this work, ViT-B-32/16 is adopted as the backbone for the visual encoder and initialized from the visual weights of CLIP [42] / BiomedCLIP [58]. A projection head is added on top of the visual encoder to bridge the gap caused by the non-pathology initialization, shown in Fig. 4. The text encoder is initialized by the pretrained knowledge encoder, as described in Sec. 3.2. In order to learn effective visual-language representation, we optimise an infoNCE contrastive objective:

$$\mathcal{L}_{\text{vt}} = -\left( \log \frac{e^{\mathbf{v}_i^T \mathbf{t}_i / \tau}}{\sum_{j=1}^n e^{\mathbf{v}_i^T \mathbf{t}_j / \tau}} + \log \frac{e^{\mathbf{t}_i^T \mathbf{v}_i / \tau}}{\sum_{j=1}^n e^{\mathbf{t}_i^T \mathbf{v}_j / \tau}} \right), \quad (6)$$

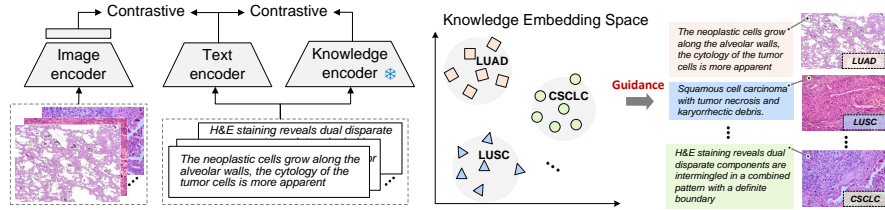


**Fig. 4:** Model architecture (left graph). A projection head is added on the top of visual encoder to bridge the gap between the image and the text encoder. The knowledge encoder is frozen across the whole training stage to distill pathology knowledge to the learnable text encoder. As a result, the pathology images can be aligned with their implicit disease labels (marked by dashed boxes in the right graph) during visual-language pretraining, since the captions contain disease attributes that have been already aligned with disease names/synonyms in the knowledge embedding space.

where  $\mathbf{v}_i = \Phi_v(x_i)$ , and  $\mathbf{t}_i = \Phi_t(c_i)$ , refer to the normalized embedding vectors from visual and text encoders, respectively.  $\tau$  denotes a temperature parameter.

**Knowledge Distillation.** To keep the alignment between images and free-form captions inside the knowledge space and thus the images can be linked to their implicit disease entities (right part in Fig. 4), we adopt an additional frozen branch to continuously distill pathology knowledge to the text encoder. Specifically, we use the text-knowledge embedding pairs to construct a contrastive loss item  $\mathcal{L}_{tk}$ , which can be computed by Eq. 6 with the normalized visual embedding vectors replaced by the knowledge embedding vectors:

$$\mathcal{L}_{tk} = -\left(\log \frac{e^{\mathbf{k}_i^T \mathbf{t}_i / \tau}}{\sum_{j=1}^n e^{\mathbf{k}_i^T \mathbf{t}_j / \tau}} + \log \frac{e^{\mathbf{t}_i^T \mathbf{k}_i / \tau}}{\sum_{j=1}^n e^{\mathbf{t}_i^T \mathbf{k}_j / \tau}}\right), \quad (7)$$

where  $\mathbf{k}_i = \Phi_k(c_i)$ , refer to the normalized embedding vectors from the knowledge encoder. The overall training loss can thus be computed as:

$$\mathcal{L} = \mathcal{L}_{vt} + \alpha \mathcal{L}_{tk}, \quad (8)$$

where  $\alpha$  denotes a weight parameter. It is worth emphasizing that the key contributions in KEP is to initialize the text encoder with the pre-obtained pathology knowledge encoder and adopt it to continuously distill pathology knowledge to the text encoder, while for the other parts, we keep the same as PLIP [23].

## 4 Experiments

In this section, we first introduce the datasets used for training and evaluation in this paper, followed by the evaluation metrics and implementation details.

### 4.1 Training Datasets.

**Dataset for Knowledge Encoding.** We carry out pathology knowledge encoding with PathKT, where 4,718 disease nodes with a total number of 50,470



attributes are extracted, including for synonyms, definitions, histological and cytological features, shown in Tab. 1.

**Datasets for KEP Pretraining.** Our dataset is composed of two parts. *First*, we collect the **OpenPath** data provided by PLIP [23] and obtain 138,874 image-text pairs after denoising and pre-processing. *Second*, we collect the **Quilt1m** [24] dataset, which gathers pathology image-text pairs from four public sources: PubMed articles, LAION [45], OpenPath [23], and Youtube videos. Since one of the downstream evaluation datasets Arch-PubMed [17] contains pathology images from PubMed articles, we remove this data source from Quilt1m to avoid data leaking. Considering that many images in Quilt1m are matched with multiple captions, we concatenate the captions related to the same image and finally obtain 576,608 image-text pairs for the Quilt1m dataset.

## 4.2 Downstream Tasks.

We evaluate the pretrained models on three tasks, namely, retrieval, zero-shot patch classification, and WSI tumor subtyping. The details for all evaluation datasets are exhibited in Supplementary Materials.

**Retrieval.** This task involves cross-modal retrieval and disease retrieval. Cross-modal retrieval aims to retrieve the correct caption for a given image and vice versa. Disease retrieval, on the other hand, utilizes the disease names to retrieve captions or images with the same disease label, which is proposed to demonstrate the effectiveness of the knowledge encoder. For cross-modal retrieval, we follow PLIP [23] to split the ARCH [17] dataset into Arch-PubMed and Arch-book. In addition, we also gather image-text pairs from publicly available educational resources and curate a retrieval dataset, termed as **PathPair**, consisting of 9,358 pathology image-caption pairs with known 1676 disease labels. For disease retrieval, we utilize the captions, images and their disease labels in PathPair.

**Zero-shot Patch Classification.** This task involves zero-shot classification on patch-level pathology images. Specifically, at inference time, we randomly select one template from the 21 templates in CONCH [36] and one type synonym from the corresponding name list (exhibited in Supplementary Materials) to yield a text prompt for each type, repeated for 100 times in every experiment. Following PLIP [23] and Quilt1m [24], we adopt these patch-level pathology image datasets: BACH [1], NCT-CRC-HE-100K [27], KatherColon [28], LC25000 [3], RenalCell [4], SICAP [48], SkinCancer [30], WSSS4LUAD [19]. Each dataset include multiple types of cell micrographs stained by Hematoxylin and Eosin.

**Zero-shot WSI Tumor Subtyping.** This task involves zero-shot tumor subtyping on pathology whole slide images. We follow MI-Zero [37] and CONCH [36] for evaluation. Specifically, we first divide WSI into  $256 \times 256$  patches and then predict the class label of each image patch in a zero-shot manner. Finally, the tumor type of the whole slide is provided by integrating Top-K predictions on patches. For this task, we also employ the templates and tumor synonyms from CONCH [36] to randomly generate 100 text prompts (listed in Supplementary materials) for each tumor type in every dataset during the inference stage. We

follow existing research [36, 37] and collect 525 WSIs with three tumor types, including 150 breast carcinoma (BRCA), 150 non-small cell lung cancer (NSCLC) histopathology slides, and 225 renal cell carcinoma (RCC) slides, from TCGA. Specifically, BRCA consists of invasive ductal carcinoma (IDC) and invasive lobular carcinoma (ILC). NSCLC consists of lung adenocarcinoma (LUAD) and lung squamous cell carcinoma (LUSC). RCC consists of chromophobe renal cell carcinoma (CHRCC), clear-cell renal cell carcinoma (CCRCC), and papillary renal cell carcinoma (PRCC). Each tumor subtype has 75 WSIs.

### 4.3 Evaluation Metrics.

**Retrieval.** To evaluate the retrieval performance, we adopt the Recall@K metric, suggesting the ratio of correctly retrieved queries in Top-K retrieved samples.

**Zero-shot Patch Classification.** For zero-shot classification tasks, we adopt the same metric as PLIP [23], namely, weighted F1 (wF1). We report the median, the first, and the third quartile (Q1, Q3) of wF1 across all text 100 prompts.

**Zero-shot WSI Tumor Subtyping.** We adopt the same metric as MI-Zero [37], namely, balanced accuracy at Top-K pooling to measure the zero-shot tumor subtyping performance on WSIs. We also report the median, the first, and the third quartile (Q1, Q3) of the balanced accuracy across all 100 text prompts.

### 4.4 Implementation Details

**Knowledge Encoder Pretraining.** We adopt the architecture of PubMedBERT [18] to encode knowledge. The embedding dimension is set to 512. The temperature parameter  $\tau$  is set to 0.04 in Eq. 2. The batch size is set to 256, including 32 disease entities with 8 instances per entity. The knowledge encoder is trained for 500 epochs.

**Pathology Image-text Pretraining.** To achieve a fair comparison with PLIP and Quilt1m, we utilize the same visual encoder (ViT-B-32) and initialization of the visual encoder (CLIP [42]), termed by KEP-32, and set the input image size to  $224 \times 224$ . Additionally, we also develop a KEP variant named KEP-16 that is initialized by the visual weights of BiomedCLIP [58] (ViT-B-16). The batch size and learning rate are set to 256 and  $1e-5$ , respectively. The temperature in Eq. 6 and Eq. 7 is set to 0.04 across all experiments. For OpenPath, we conduct the pathology VLP for 30 epochs, While for Quilt1m, 15 epochs are adopted.

## 5 Results

In this section, we show the results on the downstream tasks, to evaluate the effectiveness of proposed knowledge-enhanced representation learning. Note that for a fair comparison with the publicly available model released by the original authors, in all experiments, we separately train KEP on the OpenPath [23] dataset, and Quilt1m [24] dataset, and then report results on downstream tasks.

**Table 2:** Performance comparison with PLIP on three retrieval datasets. All models are pre-trained on the OpenPath dataset. i2t and t2i denote image-to-text and text-to-image retrieval, respectively. Bold fonts suggest the best performance.

Task	Model	Knowledge Enhancement	Arch-PubMed		Arch-book		PathPair	
			Recall@10	Recall@50	Recall@10	Recall@50	Recall@10	Recall@50
i2t	PLIP	✗	0.067	0.185	0.152	0.393	0.038	0.119
	KEP-32	✓	0.098	0.283	0.164	0.404	0.071	0.205
	KEP-16	✓	<b>0.163</b>	<b>0.398</b>	<b>0.244</b>	<b>0.537</b>	<b>0.108</b>	<b>0.275</b>
t2i	PLIP	✗	0.067	0.181	0.165	0.419	0.047	0.133
	KEP-32	✓	0.085	0.226	0.148	0.365	0.061	0.171
	KEP-16	✓	<b>0.138</b>	<b>0.339</b>	<b>0.238</b>	<b>0.533</b>	<b>0.093</b>	<b>0.247</b>

**Table 3:** Performance comparison with QuiltNet on three retrieval datasets. All models are pretrained on the Quilt1m dataset. i2t and t2i denote image-to-text and text-to-image retrieval, respectively. Bold fonts suggest the best performance.

Task	Model	Knowledge enhancement	Arch-PubMed		Arch-book		PathPair	
			Recall@10	Recall@50	Recall@10	Recall@50	Recall@10	Recall@50
i2t	QuiltNet	✗	0.139	0.326	0.188	0.407	0.065	0.166
	KEP-32	✓	0.140	0.327	0.240	0.521	0.084	0.221
	KEP-16	✓	<b>0.196</b>	<b>0.421</b>	<b>0.282</b>	<b>0.564</b>	<b>0.108</b>	<b>0.254</b>
t2i	QuiltNet	✗	0.122	0.293	0.204	0.429	0.071	0.195
	KEP-32	✓	0.135	0.326	0.275	0.568	0.106	0.276
	KEP-16	✓	<b>0.176</b>	<b>0.404</b>	<b>0.340</b>	<b>0.621</b>	<b>0.136</b>	<b>0.326</b>

## 5.1 Retrieval

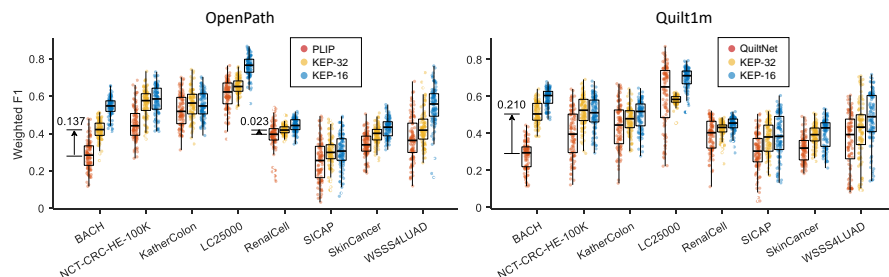
In this section, we evaluate the performance of retrieval, including cross-modal retrieval on three pathology image-caption datasets (Arch-PubMed, Arch-book, PathPair), and disease retrieval on PathPair.

**Cross-modal Retrieval.** In Tab. 2, we demonstrate the results for different models pretrained on OpenPath, KEP-32 outperforms PLIP on all datasets with respect to the image-to-text retrieval task, especially on Arch-PubMed and PathPair with more than 3% boost on R10. As for the text-to-image task, KEP-32 also achieves better performance on the dataset of Arch-PubMed and PathPair. Furthermore, our KEP-16 model improves the retrieval performance by a large margin on all datasets across both retrieval tasks. In Tab. 3, we show the performance comparison of different models pretrained on Quilt1m datasets. Similar results can be concluded that KEP-32 improves the performance on all datasets for both retrieval tasks, which demonstrates the effectiveness of knowledge guidance for visual-language pretraining on cross-modal retrieval. In summary, the knowledge enhancement is significantly effective, since KEP-32 uses the same backbone architecture of visual encoder with PLIP and Quilt1m.

**Disease Retrieval.** Tab. 4 shows the performance of disease retrieval on the PathPair dataset for different models. It can be seen that although the scale of Quilt1m is 5 times OpenPath, models pretrained on OpenPath often outperforms

**Table 4:** Performance comparison of disease retrieval. l2t and i2l denote label-to-text and image-to-label, respectively. Bold fonts suggest the best performance.

Task	Metrics	OpenPath		QuiltNet	Quilt1m	
		PLIP	KEP-32		KEP-32	KEP-16
l2t	Recall@10	0.408	0.693	0.211	0.648	0.643
	Recall@50	0.536	0.832	0.325	0.812	0.808
i2l	Recall@10	0.114	0.162	0.135	0.226	<b>0.259</b>
	Recall@50	0.292	0.381	0.322	0.473	<b>0.519</b>

**Fig. 5:** The comparison of zero-shot patch classification between different models. The left and the right subfigures suggest pretraining on OpenPath and Quilt1m, respectively. The visual encoders of KEP-32 and KEP-16 are initialized by CLIP (ViT-B-32) and BiomedCLIP (ViT-B-16), respectively. The number of points for every box is 100, with each representing the performance of one text prompt. The upper, center, and lower line of each box denote the first, median, and third quartile of the distribution.

that on Quilt1m for the label-to-text task. We conjecture this may be caused by the quality of captions in Quilt1m. Our approach KEP-32 outperforms PLIP and Quilt1m by a large margin on both label-to-text and image-to-label tasks, suggesting that the knowledge encoder contributes to paying attention to the key disease information when encoding captions, and thus improves the alignment between images and their disease labels.

## 5.2 Zero-shot Patch Classification

In this section, we evaluate the performance of zero-shot classification on patch-level pathology images from 8 datasets. We randomly generate 100 text prompts for each class and report the performance distribution (Fig. 5). Each point in the figure denotes the performance of one prompt.

**Comparison to PLIP.** In Fig. 5 (left), we demonstrate the performance comparison with PLIP [23], by only pretraining on OpenPath image-text pairs. Compared with PLIP, KEP-32 achieves better zero-shot classification performance on all datasets, with a maximum enhancement of 0.137 on the BACH dataset and a minimum improvement of 0.023 on the RenalCell dataset. Moreover, with the medical-specific initialization of the visual encoder (BiomedCLIP), KEP-16 can further improve the performance significantly in most datasets. Note that,

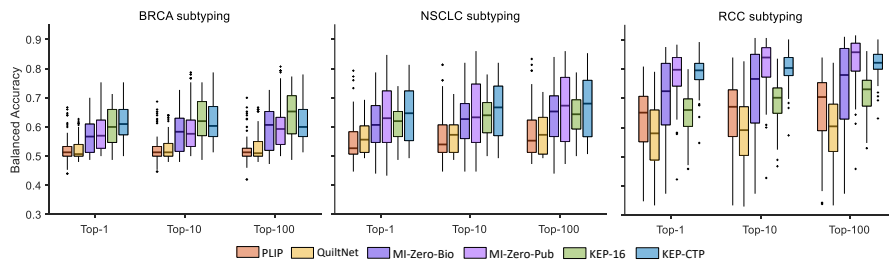


**Fig. 6:** The performance comparison of tumor subtyping on TCGA-BRCA, TCGA-NSCLC and TCGA-RCC WSIs. The upper, center, and lower line of each box denote the first, median, and third quartile of the performance distribution, respectively. The scattered points represent outliers. KEP-16 and KEP-CTP are trained on OpenPath with the visual encoder initialized by BiomedCLIP [58] and CTransPath [49], respectively. MI-Zero-Bio and MI-Zero-Pub are two variants of MI-Zero with different initialization of text encoder. Their visual encoders are initialized by CTransPath. In addition, MI-Zero adopts in-house pathology reports to pretrain their text encoders.

the boxes of KEP variants are generally shorter than that of PLIP, suggesting that our approach is less sensitive to the varying text prompts than PLIP, which can be demonstrated by the visualization of prompt embeddings, shown in Supplementary Materials.

**Comparison to QuiltNet.** As shown in Fig. 5 (right), we exhibit the performance comparison between KEP and QuiltNet [24] pretrained on Quilt1m dataset. Similar to results on OpenPath, KEP-32 outperforms Quilt1m in seven out of eight datasets, especially for the BACH, KatherColon and SkinCancer datasets. KEP-16 can further improve the weighted F1 score. Most boxes of KEP variants are also shorter than that of Quilt1m. The visualization of prompt embeddings, shown in Supplementary Materials, maintains that pathology knowledge can reduce the ambiguities of image-text alignment and thus improve the zero-shot classification performance.

### 5.3 Zero-shot WSI Tumor Subtyping

In this section, we evaluate the transfer ability of different models for tumor subtyping on three datasets of whole slide pathology images. We follow the preprocessing pipeline in MI-Zero [37] and CONCH [36], which uses CLAM [38] to segment and split each WSI into small patches.

Fig. 6 shows the performance comparison of tumor subtyping on TCGA-BRCA, TCGA-NSCLC and TCGA-RCC WSIs. MI-Zero-Bio and MI-Zero-Pub are two variants of MI-Zero with different text encoders. The visual encoders of the two MI-Zero variants are initialized by CTransPath [49], which is a pathology-specific self-supervised model pretrained on TCGA. To achieve a fair comparison, we also train a KEP variant named KEP-CTP with the visual encoder initialized with CTransPath. Both KEP-16 and KEP-CTP are trained on the OpenPath dataset. It can be seen that our approach KEP-16 and KEP-CTP outperform PLIP and QuiltNet on all datasets. Note that, the experiment

**Table 5:** Experimental results of ablation study on model architecture and initialization. Arch-PubMed and PathPair suggest the text-to-image retrieval and the disease retrieval task, respectively. PMB and KB denote PubMedBERT and our pretrained pathology knowledge encoder, respectively. BCLIP denotes BiomedCLIP. Bold fonts and underline suggest the best and the second best performance, respectively.

Visual Init.	Text Init.	Projection head	Knowledge distill	Metric loss	KatherColon Median (Q1, Q3)	Arch-PubMed R10 R50		PathPair R1 R5	
Scratch	PMB				0.322 (0.272, 0.392)	0.037	0.121	0.056	0.113
CLIP	PMB				0.407 (0.358, 0.452)	0.081	0.214	0.161	0.316
CLIP	PMB	✓			0.486 (0.448, 0.517)	0.073	0.210	0.161	0.305
BCLIP	PMB	✓			0.553 (0.503, 0.591)	<u>0.127</u>	<b>0.347</b>	0.187	0.350
CLIP	PMB	✓	✓(PMB)		0.484 (0.435, 0.520)	0.063	0.182	0.034	0.089
CLIP	KB	✓		Adasp	0.530 (0.477, 0.600)	0.086	0.232	0.270	0.482
CLIP	KB	✓	✓(KB)	Adasp	<u>0.563</u> (0.505, 0.610)	0.085	0.226	<u>0.409</u>	<b>0.618</b>
CLIP	KB	✓	✓(KB)	Triplet	0.531 (0.482, 0.580)	0.087	0.227	0.265	0.493
BCLIP	KB	✓	✓(KB)	Adasp	<b>0.580 (0.517, 0.631)</b>	<b>0.138</b>	<u>0.339</u>	<b>0.424</b>	<b>0.618</b>

**Table 6:** Experimental results of the ablation study on the loss weight  $\alpha$ . Bold fonts suggest the best performance.

$\alpha$	0.01	0.05	0.1	0.3	0.5	0.7	0.9
Median	0.531	0.524	0.531	<b>0.563</b>	0.556	0.496	0.481
Q1	0.478	0.480	0.472	<b>0.505</b>	0.497	0.447	0.428
Q3	0.589	0.587	0.571	<b>0.610</b>	0.595	0.540	0.533

comparisons between variants of KEP and MI-Zero are actually not fair for our proposed method, as the MI-Zero variants have also been pretrained on a large number of in-house data – over 550k pathology reports from hospitals [37]. Yet, KEP-CTP still outperforms MI-Zero-Bio across all datasets and achieves comparable performance with MI-Zero-Pub on NSCLC and RCC tumors.

#### 5.4 Ablation Study

In this section, we explore the impact of model architecture, initialization, and other hyperparameters, as shown in Tab. 5 and Tab. 6. Comparing the performance between different models, we can draw the following observations: (i) visual projection head can facilitate the zero-shot classification performance; (ii) our pretrained knowledge encoder can enhance the performance across all tasks; (iii) the frozen knowledge branch can further improve the performance of zero-shot classification and disease retrieval tasks while the frozen PubmedBERT can not; (iv) a better initialization of visual encoder contributes to significant performance improvement on all tasks. (v) the Adasp loss is better than the Triplet loss for the knowledge encoding. Tab. 6 shows that KEP achieves the best performance on KatherColon dataset when the loss weight  $\alpha$  is set to 0.3.

## 6 Conclusion

In this paper, we address the problem of knowledge-enhanced visual-language pretraining on computational pathology. We first curate a pathology knowledge

tree that integrates the informative attributes of diseases requiring pathological diagnosis. We then propose a novel knowledge encoding approach based on metric learning to model structured pathological knowledge. With the guidance of the pretrained knowledge encoder, we conduct extensive visual-language pre-training on pathology image-caption pairs. To demonstrate the effectiveness of our approach, we evaluate pretrained VLP models on three downstream tasks, including retrieval, zero-shot classification on patch-level pathology images, and zero-shot tumor subtyping on pathology WSIs. Quantitative experimental results demonstrate that pathology knowledge can significantly improve the performance across different tasks.

## References

1. Aresta, G., Araújo, T., Kwok, S., Chennamsetty, S.S., Safwan, M., Alex, V., Marami, B., Prastawa, M., Chan, M., Donovan, M., et al.: Bach: Grand challenge on breast cancer histology images. *Medical Image Analysis* **56**, 122–139 (2019) [9](#)
2. Bodenreider, O.: The unified medical language system (umls): integrating biomedical terminology. *Nucleic Acids Research* **32**(suppl\_1), D267–D270 (2004) [5](#)
3. Borkowski, A.A., Bui, M.M., Thomas, L.B., Wilson, C.P., DeLand, L.A., Mastorides, S.M.: Lung and colon cancer histopathological image dataset (lc25000). arXiv preprint arXiv:1912.12142 (2019) [9](#)
4. Brummer, O., Pölönen, P., Mustjoki, S., Brück, O.: Integrative analysis of histological textures and lymphocyte infiltration in renal cell carcinoma using deep learning. *bioRxiv* pp. 2022–08 (2022) [9](#)
5. Campanella, G., Hanna, M.G., Geneslaw, L., Miraflor, A., Werneck Krauss Silva, V., Busam, K.J., Brogi, E., Reuter, V.E., Klimstra, D.S., Fuchs, T.J.: Clinical-grade computational pathology using weakly supervised deep learning on whole slide images. *Nature Medicine* **25**(8), 1301–1309 (2019) [1](#)
6. Caron, M., Misra, I., Mairal, J., Goyal, P., Bojanowski, P., Joulin, A.: Unsupervised learning of visual features by contrasting cluster assignments. *Advances in Neural Information Processing Systems (NeurIPS)* **33**, 9912–9924 (2020) [4](#)
7. Chan, T.H., Cendra, F.J., Ma, L., Yin, G., Yu, L.: Histopathology whole slide image analysis with heterogeneous graph representation learning. In: *Proceedings of the IEEE/CVF Conference on Computer Vision and Pattern Recognition*. pp. 15661–15670 (2023) [1](#)
8. Chauhan, G., Liao, R., Wells, W., Andreas, J., Wang, X., Berkowitz, S., Horng, S., Szolovits, P., Golland, P.: Joint modeling of chest radiographs and radiology reports for pulmonary edema assessment. In: *International Conference on Medical Image Computing and Computer-Assisted Intervention*. pp. 529–539. Springer (2020) [3](#)
9. Chen, C., Lu, M.Y., Williamson, D.F., Chen, T.Y., Schaumberg, A.J., Mahmood, F.: Fast and scalable search of whole-slide images via self-supervised deep learning. *Nature Biomedical Engineering* **6**(12), 1420–1434 (2022) [1](#)
10. Chen, R.J., Chen, C., Li, Y., Chen, T.Y., Trister, A.D., Krishnan, R.G., Mahmood, F.: Scaling vision transformers to gigapixel images via hierarchical self-supervised learning. In: *Proceedings of the IEEE/CVF Conference on Computer Vision and Pattern Recognition*. pp. 16144–16155 (2022) [1](#)
11. Chen, X., Fan, H., Girshick, R., He, K.: Improved baselines with momentum contrastive learning. arXiv preprint arXiv:2003.04297 (2020) [4](#)

12. Chen, Y.C., Li, L., Yu, L., El Kholy, A., Ahmed, F., Gan, Z., Cheng, Y., Liu, J.: Uniter: Learning universal image-text representations (2019) [3](#)
13. Chen, Y.C., Lu, C.S.: Rankmix: Data augmentation for weakly supervised learning of classifying whole slide images with diverse sizes and imbalanced categories. In: Proceedings of the IEEE/CVF Conference on Computer Vision and Pattern Recognition. pp. 23936–23945 (2023) [1](#)
14. Chen, Z., Li, G., Wan, X.: Align, reason and learn: Enhancing medical vision-and-language pre-training with knowledge. In: Proceedings of the 30th ACM International Conference on Multimedia. pp. 5152–5161 (2022) [3](#)
15. Chen, Z., Song, Y., Chang, T.H., Wan, X.: Generating radiology reports via memory-driven transformer. In: Proceedings of the 2020 Conference on Empirical Methods in Natural Language Processing (EMNLP). pp. 1439–1449 (2020) [4](#)
16. Cui, H., Xu, Y., Li, W., Wang, L., Duh, H.: Collaborative learning of cross-channel clinical attention for radiotherapy-related esophageal fistula prediction from ct. In: International Conference on Medical Image Computing and Computer-Assisted Intervention. pp. 212–220. Springer (2020) [4](#)
17. Gamper, J., Rajpoot, N.: Multiple instance captioning: Learning representations from histopathology textbooks and articles. In: Proceedings of the IEEE/CVF Conference on Computer Vision and Pattern Recognition. pp. 16549–16559 (2021) [9](#)
18. Gu, Y., Tinn, R., Cheng, H., Lucas, M., Usuyama, N., Liu, X., Naumann, T., Gao, J., Poon, H.: Domain-specific language model pretraining for biomedical natural language processing. *ACM Transactions on Computing for Healthcare (HEALTH)* **3**(1), 1–23 (2021) [10](#)
19. Han, C., Pan, X., Yan, L., Lin, H., Li, B., Yao, S., Lv, S., Shi, Z., Mai, J., Lin, J., et al.: Wsss4luad: Grand challenge on weakly-supervised tissue semantic segmentation for lung adenocarcinoma. arXiv preprint arXiv:2204.06455 (2022) [9](#)
20. Hermans, A., Beyer, L., Leibe, B.: In defense of the triplet loss for person re-identification. arXiv preprint arXiv:1703.07737 (2017) [7](#)
21. Huang, S.C., Shen, L., Lungren, M.P., Yeung, S.: Gloria: A multimodal global-local representation learning framework for label-efficient medical image recognition. In: Proceedings of the IEEE/CVF International Conference on Computer Vision. pp. 3942–3951 (2021), official Implementation: <https://github.com/marshuang80/gloria> [3](#)
22. Huang, X., Fang, Y., Lu, M., Yan, F., Yang, J., Xu, Y.: Dual-ray net: automatic diagnosis of thoracic diseases using frontal and lateral chest x-rays. *Journal of Medical Imaging and Health Informatics* **10**(2), 348–355 (2020) [4](#)
23. Huang, Z., Bianchi, F., Yuksekgonul, M., Montine, T.J., Zou, J.: A visual–language foundation model for pathology image analysis using medical twitter. *Nature medicine* **29**(9), 2307–2316 (2023) [2](#), [3](#), [8](#), [9](#), [10](#), [12](#)
24. Ikezogwo, W., Seyfioglu, S., Ghezloo, F., Geva, D., Sheikh Mohammed, F., Anand, P.K., Krishna, R., Shapiro, L.: Quilt-1m: One million image-text pairs for histopathology. *Advances in Neural Information Processing Systems* **36** (2024) [2](#), [3](#), [9](#), [10](#), [13](#)
25. Jia, C., Yang, Y., Xia, Y., Chen, Y.T., Parekh, Z., Pham, H., Le, Q., Sung, Y.H., Li, Z., Duerig, T.: Scaling up visual and vision-language representation learning with noisy text supervision. In: International Conference on Machine Learning. pp. 4904–4916. PMLR (2021) [2](#)



26. Kang, M., Song, H., Park, S., Yoo, D., Pereira, S.: Benchmarking self-supervised learning on diverse pathology datasets. In: Proceedings of the IEEE/CVF Conference on Computer Vision and Pattern Recognition (CVPR). pp. 3344–3354 (2023) [1](#), [3](#)
27. Kather, J.N., Halama, N., Marx, A.: 100,000 histological images of human colorectal cancer and healthy tissue. Zenodo10 **5281** (2018) [9](#)
28. Kather, J.N., Krisam, J., Charoentong, P., Luedde, T., Herpel, E., Weis, C.A., Gaiser, T., Marx, A., Valous, N.A., Ferber, D., et al.: Predicting survival from colorectal cancer histology slides using deep learning: A retrospective multicenter study. PLoS Medicine **16**(1), e1002730 (2019) [9](#)
29. Kim, W., Son, B., Kim, I.: Vilt: Vision-and-language transformer without convolution or region supervision. In: International Conference on Machine Learning. pp. 5583–5594. PMLR (2021) [3](#)
30. Kriegsmann, K., Lobers, F., Zgorzelski, C., Kriegsmann, J., Janssen, C., Meliss, R.R., Muley, T., Sack, U., Steinbuss, G., Kriegsmann, M.: Deep learning for the detection of anatomical tissue structures and neoplasms of the skin on scanned histopathological tissue sections. Frontiers in Oncology **12**, 1022967 (2022) [9](#)
31. Kundra, R., Zhang, H., Sheridan, R., Sirintrapun, S.J., Wang, A., Ochoa, A., Wilson, M., Gross, B., Sun, Y., Madupuri, R., et al.: Oncotree: a cancer classification system for precision oncology. JCO clinical cancer informatics **5**, 221–230 (2021) [3](#), [5](#)
32. Li, H., Zhu, C., Zhang, Y., Sun, Y., Shui, Z., Kuang, W., Zheng, S., Yang, L.: Task-specific fine-tuning via variational information bottleneck for weakly-supervised pathology whole slide image classification. In: Proceedings of the IEEE/CVF Conference on Computer Vision and Pattern Recognition. pp. 7454–7463 (2023) [1](#)
33. Li, M., Cai, W., Verspoor, K., Pan, S., Liang, X., Chang, X.: Cross-modal clinical graph transformer for ophthalmic report generation. In: Proceedings of the IEEE/CVF Conference on Computer Vision and Pattern Recognition. pp. 20656–20665 (2022) [4](#)
34. Lin, T., Yu, Z., Hu, H., Xu, Y., Chen, C.W.: Interventional bag multi-instance learning on whole-slide pathological images. In: Proceedings of the IEEE/CVF Conference on Computer Vision and Pattern Recognition. pp. 19830–19839 (2023) [1](#)
35. Lin, W., Zhao, Z., Zhang, X., Wu, C., Zhang, Y., Wang, Y., Xie, W.: Pmc-clip: Contrastive language-image pre-training using biomedical documents. In: International Conference on Medical Image Computing and Computer-Assisted Intervention (MICCAI) (2023) [3](#)
36. Lu, M.Y., Chen, B., Williamson, D.F., Chen, R.J., Liang, I., Ding, T., Jaume, G., Odintsov, I., Zhang, A., Le, L.P., et al.: Towards a visual-language foundation model for computational pathology. arXiv preprint arXiv:2307.12914 (2023) [2](#), [3](#), [9](#), [10](#), [13](#), [7](#), [8](#)
37. Lu, M.Y., Chen, B., Zhang, A., Williamson, D.F., Chen, R.J., Ding, T., Le, L.P., Chuang, Y.S., Mahmood, F.: Visual language pretrained multiple instance zero-shot transfer for histopathology images. In: Proceedings of the IEEE/CVF Conference on Computer Vision and Pattern Recognition. pp. 19764–19775 (2023) [2](#), [3](#), [9](#), [10](#), [13](#), [14](#)
38. Lu, M.Y., Williamson, D.F., Chen, T.Y., Chen, R.J., Barbieri, M., Mahmood, F.: Data-efficient and weakly supervised computational pathology on whole-slide images. Nature Biomedical Engineering **5**(6), 555–570 (2021) [1](#), [13](#)
39. McInnes, L., Healy, J., Melville, J.: Umap: Uniform manifold approximation and projection for dimension reduction. arXiv preprint arXiv:1802.03426 (2018) [5](#)

40. Müller, P., Kaissis, G., Zou, C., Rueckert, D.: Joint learning of localized representations from medical images and reports. In: European Conference on Computer Vision. pp. 685–701. Springer (2022) [3](#)
41. Neumann, M., King, D., Beltagy, I., Ammar, W.: ScispaCy: Fast and robust models for biomedical natural language processing. In: Demner-Fushman, D., Cohen, K.B., Ananiadou, S., Tsujii, J. (eds.) Proceedings of the 18th BioNLP Workshop and Shared Task. pp. 319–327. Association for Computational Linguistics, Florence, Italy (Aug 2019). <https://doi.org/10.18653/v1/W19-5034>, <https://aclanthology.org/W19-5034> [5](#)
42. Radford, A., Kim, J.W., Hallacy, C., Ramesh, A., Goh, G., Agarwal, S., Sastry, G., Askell, A., Mishkin, P., Clark, J., et al.: Learning transferable visual models from natural language supervision. In: International Conference on Machine Learning. pp. 8748–8763. PMLR (2021) [2](#), [3](#), [7](#), [10](#)
43. Roberts, R.J.: Pubmed central: The genbank of the published literature (2001) [2](#)
44. Rorke, L.B.: Pathologic diagnosis as the gold standard (1997) [1](#)
45. Schuhmann, C., Beaumont, R., Vencu, R., Gordon, C., Wightman, R., Cherti, M., Coombs, T., Katta, A., Mullis, C., Wortsman, M., et al.: Laion-5b: An open large-scale dataset for training next generation image-text models. *Advances in Neural Information Processing Systems* **35**, 25278–25294 (2022) [9](#)
46. Shaban, M., Awan, R., Fraz, M.M., Azam, A., Tsang, Y.W., Snead, D., Rajpoot, N.M.: Context-aware convolutional neural network for grading of colorectal cancer histology images. *IEEE Transactions on Medical Imaging* **39**(7), 2395–2405 (2020) [1](#)
47. Shao, Z., Bian, H., Chen, Y., Wang, Y., Zhang, J., Ji, X., et al.: Transmil: Transformer based correlated multiple instance learning for whole slide image classification. *Advances in Neural Information Processing Systems* **34**, 2136–2147 (2021) [1](#)
48. Silva-Rodríguez, J., Colomer, A., Sales, M.A., Molina, R., Naranjo, V.: Going deeper through the gleason scoring scale: An automatic end-to-end system for histology prostate grading and cribriform pattern detection. *Computer Methods and Programs in Biomedicine* **195**, 105637 (2020) [9](#)
49. Wang, X., Yang, S., Zhang, J., Wang, M., Zhang, J., Yang, W., Huang, J., Han, X.: Transformer-based unsupervised contrastive learning for histopathological image classification. *Medical Image Analysis* **81**, 102559 (2022) [1](#), [13](#), [3](#)
50. Wu, C., Zhang, X., Zhang, Y., Wang, Y., Xie, W.: Medklip: Medical knowledge enhanced language-image pre-training. *medRxiv* pp. 2023–01 (2023) [3](#)
51. Xie, X., Niu, J., Liu, X., Chen, Z., Tang, S., Yu, S.: A survey on incorporating domain knowledge into deep learning for medical image analysis. *Medical Image Analysis* **69**, 101985 (2021) [3](#)
52. Xu, H., Ghosh, G., Huang, P.Y., Okhonko, D., Aghajanyan, A., Metze, F., Zettlemoyer, L., Feichtenhofer, C.: Videoclip: Contrastive pre-training for zero-shot video-text understanding. In: Proceedings of the 2021 Conference on Empirical Methods in Natural Language Processing. pp. 6787–6800 (2021) [3](#)
53. Xuan, H., Stylianou, A., Liu, X., Pless, R.: Hard negative examples are hard, but useful. In: Computer Vision–ECCV 2020: 16th European Conference, Glasgow, UK, August 23–28, 2020, Proceedings, Part XIV 16. pp. 126–142. Springer (2020) [7](#)
54. Yang, S., Wu, X., Ge, S., Zhou, S.K., Xiao, L.: Knowledge matters: Chest radiology report generation with general and specific knowledge. *Medical Image Analysis* **80**, 102510 (2022) [4](#)

55. Yu, F., Tang, J., Yin, W., Sun, Y., Tian, H., Wu, H., Wang, H.: Ernie-vil: Knowledge enhanced vision-language representations through scene graphs. In: Proceedings of the AAAI Conference on Artificial Intelligence. vol. 35, pp. 3208–3216 (2021) [4](#)
56. Yu, J., Wang, Z., Vasudevan, V., Yeung, L., Seyedhosseini, M., Wu, Y.: Coca: Contrastive captioners are image-text foundation models. arXiv preprint arXiv:2205.01917 (2022) [3](#)
57. Zbontar, J., Jing, L., Misra, I., LeCun, Y., Deny, S.: Barlow twins: Self-supervised learning via redundancy reduction. In: International Conference on Machine Learning (ICML). pp. 12310–12320. PMLR (2021) [4](#)
58. Zhang, S., Xu, Y., Usuyama, N., Bagga, J., Tinn, R., Preston, S., Rao, R., Wei, M., Valluri, N., Wong, C., et al.: Large-scale domain-specific pretraining for biomedical vision-language processing. arXiv preprint arXiv:2303.00915 (2023) [3](#), [7](#), [10](#), [13](#)
59. Zhang, X., Wu, C., Zhang, Y., Xie, W., Wang, Y.: Knowledge-enhanced visual-language pre-training on chest radiology images. Nature Communications **14**(1), 4542 (2023) [3](#)
60. Zhang, Y., Jiang, H., Miura, Y., Manning, C.D., Langlotz, C.P.: Contrastive learning of medical visual representations from paired images and text. In: Machine Learning for Healthcare (2022), highest Starred Implementation: <https://github.com/edreisMD/ConVIRT-pytorch> [3](#)
61. Zhou, X., Zhong, Y., Cheng, Z., Liang, F., Ma, L.: Adaptive sparse pairwise loss for object re-identification. In: Proceedings of the IEEE/CVF Conference on Computer Vision and Pattern Recognition. pp. 19691–19701 (2023) [6](#)

## Supplementary Material

This Supplementary Material contains the following parts:

**1. Dataset statistics.**

The summary of datasets used in this paper.

**2. Additional Results on Zero-shot WSI Tumor Subtyping.**

Additional results on zero-shot WSI tumor subtyping for KEP variants pre-trained on Quilt1m and KEP variants with CNN-based visual encoders.

**3. Discussion.**

Details and discussion about the soft version of max-min positive similarity, frozen knowledge encoder and robustness towards text prompts.

**4. Text Prompts.**

The list of text prompts used in this paper.

## 1 Dataset statistics

**Table S1:** Statistics of test datasets utilized in this work. Classification suggests patch-level zero-shot image classification and Subtyping denotes zero-shot WSI tumor subtyping.

Task	Dataset	#images	#types	tissue
Retrieval	Arch-PubMed	1923	–	Multiple
	Arch-book	1306	–	Multiple
	PathPair	9,358	1676	Multiple
Classification	BACH	400	4	Breast
	NCT-CRC-HE-100K	100K	9	Colorectal
	KatherColon	7,180	9	Colon
	LC25000	25K	5	Lung, Colon
	RenalCell	36,687	5	Renal
	SICAP	12,081	4	Prostate
	SkinCancer	129,369	16	Skin
WSSS4LUAD	4,693	3	Lung	
Subtyping	TCGA-BRCA	150	2	Breast
	TCGA-NSCLC	150	2	Lung
	TCGA-RCC	225	3	Renal

## 2 Additional Results on Zero-shot WSI Tumor Subtyping

In this section, we provide additional results on zero-shot WSI tumor subtyping for the KEP variants that are pretrained on Quilt1m, as shown in Fig. S1. It can be seen that KEP-16 achieves better performance than QuiltNet on BRCA and NSCLC datasets. KEP-CTP can further improve the performance, especially on RCC dataset.

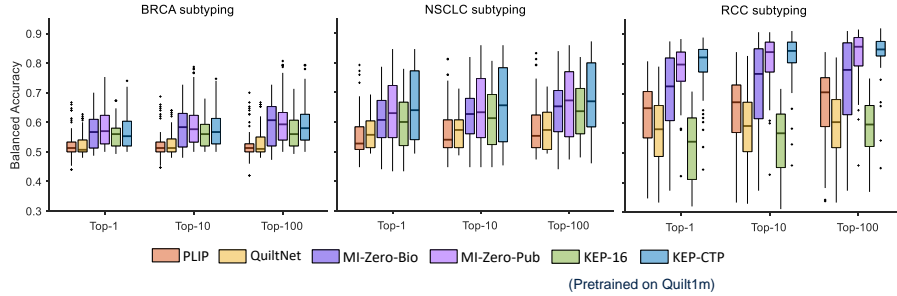


**Fig. S1:** The performance comparison of tumor subtyping on TCGA-BRCA, TCGA-NSCLC and TCGA-RCC WSIs. The upper, center, and lower line of each box denote the first, median, and third quartile of the performance distribution, respectively. The scattered points represent outliers. KEP-16 and KEP-CTP are trained on Quilt1m with the visual encoder initialized by BiomedCLIP [58] and CTransPath [49], respectively.

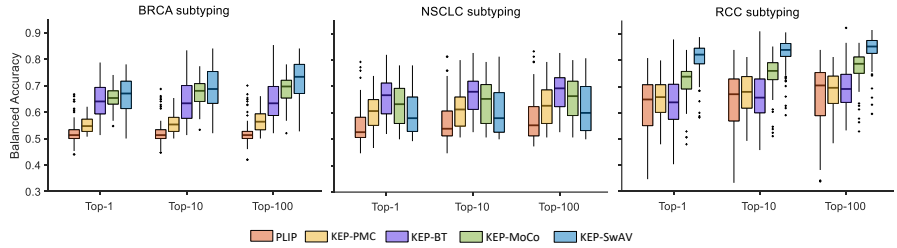


**Fig. S2:** The performance comparison of tumor subtyping on TCGA-BRCA, TCGA-NSCLC and TCGA-RCC WSIs. The upper, center, and lower line of each box denote the first, median, and third quartile of the performance distribution, respectively. The scattered points represent outliers. KEP-PMC is trained on OpenPath with the visual encoder initialized by PMC-CLIP [35], KEP-BT, KEP-MoCo, and KEP-SwAV are trained on OpenPath with the visual encoder initialized by PathSSL-BT, PathSSL-MoCo, and PathSSL-SwAV [26], respectively.

Furthermore, we change the backbone of KEP’s visual encoder to convolutional neural networks and initialize it with PMC-CLIP [35] and PathSSL [26]. PMC-CLIP refers to a visual-language model pretrained on medical image-text pairs crawled from PubMed papers. PathSSL consists of PathSSL-BT, PathSSL-MoCo, and PathSSL-SwAV, which are self-supervised models pretrained on

TCGA pathology images with different SSL strategies, including Barlow Twins [57], MoCo v2 [11], and SwAV [6]. Except for the visual encoder, all training details are consistent with the main text.

Fig. S2 shows the performance comparison between PLIP and different KEP variants pretrained on OpenPath. It can be seen that almost all KEP variants outperform PLIP on all datasets, suggesting that our pretraining approach can seamlessly generalize to CNN-based visual encoders with the same parameter configuration. In particular, KEP-MoCo and KEP-SwAV significantly improve the subtyping performance on breast and renal tumors.

### 3 Discussion

*Soft Version of Max-min Positive Similarity.*

$$S_i^+ = \max_p \min_q \langle \mathbf{z}_p^i, \mathbf{z}_q^i \rangle \approx \tau \log \left( \sum_{p=1}^k e^{\frac{\min_q \langle \mathbf{z}_p^i, \mathbf{z}_q^i \rangle}{\tau}} \right) \quad (\text{S1})$$

$$\min_q \langle \mathbf{z}_p^i, \mathbf{z}_q^i \rangle \approx -\tau \log \left( \sum_{q=1}^k e^{-\frac{\langle \mathbf{z}_p^i, \mathbf{z}_q^i \rangle}{\tau}} \right) \quad (\text{S2})$$

$$S_i^+ \approx \tau \log \left( \sum_{p=1}^k \frac{1}{\sum_{q=1}^k e^{-\frac{\langle \mathbf{z}_p^i, \mathbf{z}_q^i \rangle}{\tau}}} \right) \quad (\text{S3})$$

*Frozen Knowledge Encoder.* Here, we discuss the advantages of the frozen knowledge encoder. Although the visual-language pretraining can start in a well-defined pathology embedding space curated by the knowledge initialization of the text encoder, the free text from the training pairs may impair the knowledge structure built from the pathology knowledge tree, leading to overfitting on the training image-text pairs. As a consequence, the frozen knowledge encoder across the entire training period holds two advantages: (i) the text embedding from this branch acts as a frozen knowledge continuously distilling to the active text encoder, which, therefore, can substantially keep the entire alignment procedure in the well-structured knowledge embedding space; (ii) the additional contrastive loss between the active text encoder and this branch serves as a regularization term to prevent the overfitting problem.

*Robustness towards Text Prompts.* To show the robustness of our approach towards different text prompts, we use UMAP [39] to visualize the prompt embeddings for each class, as shown in Fig. S3. It can be concluded that the prompt embeddings of PLIP and QuiltNet suffer from high similarities between different classes, especially in the dataset of BACH, LC25000, SICAP, and WSSS4LUAD, which therefore causes large ambiguities for zero-shot classification. In contrast, the embeddings generated by our proposed frozen knowledge encoder (denoted as Knowledge encoder), are well-separated in most datasets. With the knowledge guidance, the text encoder of KEP, denoted by KEP-32, also outputs well-separated prompt embeddings of different classes, suggesting that pathology knowledge can substantially improve the structure of text embedding space.



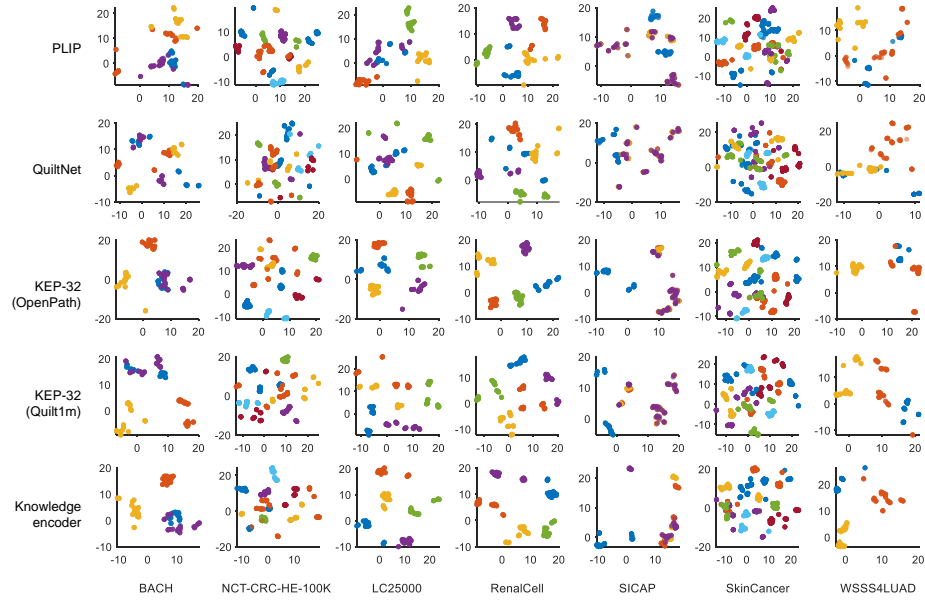


**Fig. S3:** The UMAP visualization of prompt embeddings on different datasets. Each color represents a class of the dataset and consists of 100 points corresponding to the random 100 prompts for each category. NCT-CRC-HE-100K and KatherColon share the same text prompts. KEP-32 (OpenPath) and KEP-32 (Quilt1m) denote the prompt embeddings generated from the text encoder pretrained on the dataset of OpenPath and Quilt1m, respectively. Knowledge encoder denotes the prompt embeddings from the frozen knowledge encoder.

## 4 Text Prompts

In this section, we list all text prompts used in this paper. The templates are shown in Tab. S2. The synonyms for patch-level dataset are shown in Tab. S3-S9. The class names for TCGA WSIs are exhibited in Tab. S10-S12.

**Table S2:** Prompt templates used in this paper, which are consistent with CONCH [36], CLASSNAME is replaced by the names/synonyms of classes.

---

CLASSNAME.
a photomicrograph showing CLASSNAME.
a photomicrograph of CLASSNAME.
an image of CLASSNAME.
an image showing CLASSNAME.
an example of CLASSNAME.
CLASSNAME is shown.
this is CLASSNAME.
there is CLASSNAME.
a histopathological image showing CLASSNAME.
a histopathological image of CLASSNAME.
a histopathological photograph of CLASSNAME.
a histopathological photograph showing CLASSNAME.
shows CLASSNAME.
presence of CLASSNAME.
CLASSNAME is present.
an H&E stained image of CLASSNAME.
an H&E stained image showing CLASSNAME.
an H&E image showing CLASSNAME.
an H&E image of CLASSNAME.
CLASSNAME, H&E stain.
CLASSNAME, H&E.

---

**Table S3:** Class names of BACH.

Class	Names/Synonyms
Benign	breast non-malignant benign tissue; breast benign tissue; non-malignant benign tissue of breast
InSitu	breast malignant in-situ carcinoma; breast in-situ carcinoma; malignant carcinoma in-situ of breast
Invasive	breast malignant invasive carcinoma; breast invasive carcinoma; invasive carcinoma of breast
Normal	normal breast tissue; breast normal tissue; breast non-cancerous tissue

**Table S4:** Class names of NCT-CRC-HE-100K and KatherColon from CONCH [36].

Class	Names/Synonyms
ADI	adipose; adipose tissue; adipocytes; fat; fat cells
BACK	background; penmarking; empty space; background artifacts
DEB	debris; colorectal adenocarcinoma debris and necrosis; necrosis; necrotic debris
LYM	lymphocytes; lymphoid aggregate; immune cells; lymphoid infiltrate; inflammatory cells
MUC	mucus; mucin; mucus pool; mucin pool
MUS	smooth muscle; smooth muscle tissue; muscle; muscularis propria; muscularis mucosa
NORM	normal colon mucosa; uninvolved colon mucosa; benign colon mucosa; benign epithelium
STR	cancer-associated stroma; tumor-associated stroma; stromal cells; stromal tissue; stroma
TUM	colorectal adenocarcinoma epithelium; colorectal adenocarcinoma; tumor; adenocarcinoma; malignant epithelium

**Table S5:** Class names of LC25000.

Class	Names/Synonyms
lung_aca	lung adenocarcinoma; adenocarcinoma of the lung; lung cancer, adenocarcinoma
lung_n	benign lung; benign lung tissues; non-malignant lung tissue
lung_scc	lung squamous cell carcinoma; squamous-cell carcinoma of the lung; squamous cell lung cancer
colon_aca	colon adenocarcinoma; adenocarcinoma of the colon; colon cancer, adenocarcinoma
colon_n	benign colon; benign colonic tissue; non-malignant colon tissue

**Table S6:** Class names of RenalCell.

Class	Names/Synonyms
blood	red blood cells; red blood corpuscles; red cells; erythroid cells
cancer	non-tumor; normal tissue; non-cancerous tissue
normal renal cancer;	renal tumor; renal neoplasm; renal carcinoma
other	torn adipose necrotic tissue; torn adipose tissue, necrosis; adipose necrotic tissue
stroma	muscle fibrous stroma blood vessels; blood vessels, muscle fibrous stroma; muscle fibers and blood vessels in stroma

**Table S7:** Class names of SICAP from CONCH [36].

Class	Names/Synonyms
NC	non-cancerous tissue; non-cancerous prostate tissue; benign tissue; benign glands; benign prostate tissue; benign prostate glands
G3	gleason grade 3; gleason pattern 3; prostate cancer, gleason grade 3; prostate cancer, gleason pattern 3; prostate adenocarcinoma, well-differentiated; well-differentiated prostatic adenocarcinoma
G4	gleason grade 4; gleason pattern 4; prostate cancer, gleason grade 4; prostate cancer, gleason pattern 4; prostate adenocarcinoma, moderately differentiated; moderately differentiated prostatic adenocarcinoma
G5	gleason grade 5; gleason pattern 5; prostate cancer, gleason grade 5; prostate cancer, gleason pattern 5; prostate adenocarcinoma, poorly differentiated; poorly differentiated prostatic adenocarcinoma
Tumor	prostatic adenocarcinoma; adenocarcinoma; prostate cancer; tumor tissue; cancerous tissue

**Table S8:** Class names of WSSS4LUAD from CONCH [36].

Class	Names/Synonyms
normal	non-tumor; normal tissue; non-cancerous tissue
stroma	tumor-associated stroma; cancer-associated stroma; tumor-associated stromal tissue; cancer-associated stromal tissue
tumor	tumor tissue; tumor epithelial tissue; cancerous tissue

**Table S9:** Class names of SkinCancer.

Class	Names/Synonyms
necrosis	necrosis; necrotic tissue; necrotic cells
skeletal	skeletal muscle; skeletal muscle cells; skeletal muscle tissue
sweatglands	eccrine sweat glands; merocrine glands; skin eccrine sweat glands
vessel	vessels; blood vessels; vessel
elastosis	elastosis; elastosis of skin; skin elastosis
chondraltissue	chondral tissue; chondral tissue of skin; skin chondral tissue
hairfollicle	hair follicle; hair follicle of skin; skin hair follicle
epidermis	epidermis; skin epidermis; epidermal cells
nerves	nerves; nerve fibers; nerve axons
subcutis	subcutis; subcutaneous tissue; skin subcutis; hypodermis; hypoderm
dermis	dermis; skin dermis; corium; skin corium
sebaceousglands	sebaceous; sebaceous gland; skin sebaceous
sqcc	squamous-cell carcinoma; cutaneous squamous-cell carcinoma; squamous-cell carcinoma of the skin; squamous-cell skin cancer
melanoma	melanoma in-situ; malignant melanoma; cutaneous melanoma
bcc	basal-cell carcinoma; basal-cell cancer; basal-cell tumor
naevus	naevus; mole; skin nevus

**Table S10:** Class names of TCGA-BRCA, which are consistent with CONCH [36].

Class	Names/synonyms
IDC	invasive ductal carcinoma; breast invasive ductal carcinoma; invasive ductal carcinoma of the breast; invasive carcinoma of the breast, ductal pattern; breast IDC
ILC	invasive lobular carcinoma; breast invasive lobular carcinoma; invasive lobular carcinoma of the breast; invasive carcinoma of the breast, lobular pattern; breast ILC

**Table S11:** Class names of TCGA-NSCLC, which are consistent with CONCH [36].

Class	Names/synonyms
LUAD	adenocarcinoma; lung adenocarcinoma; adenocarcinoma of the lung; LUAD
LUSC	squamous cell carcinoma; lung squamous cell carcinoma; squamous cell carcinoma of the lung; LUSC

**Table S12:** Class names of TCGA-RCC, which are consistent with CONCH [36].

Class	Names/synonyms
CCRCC	clear cell renal cell carcinoma; renal cell carcinoma, clear cell type; renal cell carcinoma of the clear cell type; clear cell RCC
PRCC	papillary renal cell carcinoma; renal cell carcinoma, papillary type; renal cell carcinoma of the papillary type; papillary RCC
CHRCC	chromophobe renal cell carcinoma; renal cell carcinoma, chromophobe type; renal cell carcinoma of the chromophobe type; chromophobe RCC